Experimental and numerical investigation of the nonlinear dynamics of compliant mechanisms for deployable structures

Florence Dewalque[a], **Cédric Schwartz**[b], **Vincent Denoël**[b], **Jean-Louis Croisier**[b], **Bénédicte Forthomme**[b], **Olivier Brüls**[ab]

[a]*Department of Aerospace and Mechanical Engineering, University of Liège*
[b]*Laboratory of Human Motion Analysis, University of Liège*
Allée de la Découverte 9 (B52/3), 4000 Liège, Belgium
`f.dewalque@ulg.ac.be`

Abstract

This paper studies the dynamics of tape springs which are characterised by a highly geometrical nonlinear behaviour including buckling, the formation of folds and hysteresis. An experimental set-up is designed to capture these complex nonlinear phenomena. The experimental data are acquired by the means of a 3D motion analysis system combined with a synchronised force plate. Deployment tests show that the motion can be divided into three phases characterised by different types of folds, frequencies of oscillation and damping behaviours. Furthermore, the reproducibility quality of the dynamic and quasi-static results is validated by performing a large number of tests. In parallel, a nonlinear finite element model is developed. The required model parameters are identified based on simple experimental tests such as static deformed configurations and small amplitude vibration tests. In the end, the model proves to be well correlated with the experimental results in opposite sense bending, while in equal sense, both the experimental set-up and the numerical model are particularly sensitive to the initial conditions.

Keywords: Tape springs, Nonlinear dynamics, Finite element simulations, Structural damping, Experimental tests, Model correlation.

1 Introduction

Compliant mechanisms rely on the deformation of flexible structural components to produce motion. Based on this behaviour, several advantageous characteristics can be put forward compared to common kinematic joints: the storage of energy creating a restoring force, the deformations staying in the elastic regime, the small number of required parts, often limited to a single one, the limited impact or absence of assembly procedure, the absence of gap affecting the accuracy in measurement systems, the combination of the guiding and motor functions, and the absence of friction resulting in the absence of wear and lubrication [1]. In terms of applications, compliant elements can be found in various domains, for example in constant-force mechanisms [2], in electrical contacts [3], in robotic orthoses [4], in grippers [5], in the auto-focusing mechanism of cameras [6], in atomic force microscopes [7] and in deployable structures [8]. Finally, compliant mechanisms can be designed using topology optimisation methods [1, 5, 9].

High-fidelity structural models are then required to reach a detailed understanding of compliant mechanisms characteristics and predict their evolution in various situations. In order to reach a high level of accuracy, experimental data are essential to provide inputs for the models and validate their resulting outputs. In this work, an experimental and numerical investigation is performed on compliant mechanisms called tape springs, whose nonlinearity is mainly geometric due to their transverse curvature. Even though they generally operate in the elastic regime, their behaviour is characterised by geometrically nonlinear phenomena such as buckling, the formation of folds and hysteresis, some energy being dissipated every time a fold disappears. In the end, these characteristics lead to attractive features for deployable structures such as self-actuation and self-locking in the unfolded configuration.

Tape springs are mainly used in space deployable structures for satellites. Indeed, they represent simple, autonomous, robust and easy-to-integrate components compared to common mechanisms usually composed of several kinematic joints set into motion by the means of motors. Successful uses of tape springs can be found in several space missions such as the six MYRIADE micro-satellites for the deployment of solar arrays, antennas and masts [10] or the MARS EXPRESS spacecraft for the deployment of a long wavelength antenna [11] and will be found in future missions such as SOLAR ORBITER for the deployment of a radio and plasma wave antenna or NORSAT-1 for the deployment of an AIS (Automatic Identification System) receiver. They are also considered as support structures for the deployment of Cassegrain telescopes [12], inflatable

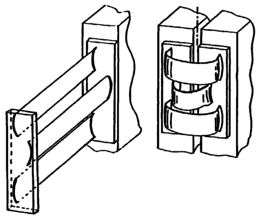

Figure 1: MAEVA hinge [17].

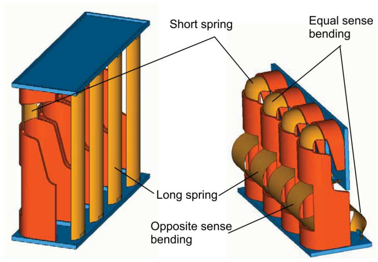

Figure 2: Hinge designed by Boesch *et al.* [18].

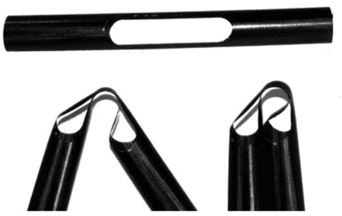

Figure 3: Integral slotted hinge [19].

structures [13] and solar sails [14, 15].

The inherent characteristics of tape springs exploited in these applications are the following. First of all, when deformed to reach their folded configuration, the deformations stay in the elastic regime, provided that the geometric and material parameters satisfy a design constraint [16]. The stored elastic energy is then responsible for a residual bending moment that leads to a passive and self-actuated deployment until the tape springs reach their equilibrium state which, in the context of this work, is the straight stress-free configuration. In some other applications, several stable configurations may coexist [8]. Furthermore, compared to kinematic joints which usually imply some sliding between contact surfaces while in motion, the deployment of tape springs only leads to the deformation of structural elements. The use of lubricant is then irrelevant in this case and the risks of outgassing or contamination are limited in space. At the buckling point, one observes a transition from a configuration characterised by a high stiffness to a folded one associated with a low stiffness. Because of this low post-buckling stiffness, large motion amplitudes can be encountered and have to be constrained in order to avoid collisions with other components. Likewise, the shocks created by the formation or the disappearance of folds have to be monitored to limit the interference with other sensitive instruments. Finally, several tape springs can easily be combined to form a hinge with characteristics specific to the application at hand, showing thus the versatility of these compliant mechanisms. For example, the MAEVA hinge is composed of three tape springs with alternate orientations [17] (Figure 1), Boesch *et al.* designed a hinge with four pairs of tape springs, each one being composed of a long and a short element [18] (Figure 2). The assets of tape springs can also be found in hinges consisting of thin walled tubes with longitudinal holes which are called integral slotted hinges [11, 19] (Figure 3).

To capture and predict the nonlinear behaviour of tape springs, analytical developments, finite element analyses and experimental tests are performed. Theoretical developments were first derived by Wüst [20], Rimrott [21] and Mansfield [22]. Various analytical models were developed afterwards: in [23], tape springs are represented as two rigid bodies of variable length interconnected by a mobile hinge; in [24], a variational approach expressed in terms of potential energy is used to perform quasi-static analyses; in [25, 26], a one-dimensional planar rod model with a flexible cross-section is investigated; in [27], a viscoelastic analytical model representing three aspects (stowage, stability and deployment) of bistable tape springs is developed; in [28, 29], the equations of motion for the deployment of solar panels with tape springs are derived through a path-dependent path identification method combined with dynamic equations and based on a rigid multi-body theory in [30].

Regarding finite element models, comprehensive quasi-static analyses were performed in order to understand the impact of the geometric and material parameters on the relationship linking the bending moment and the rotation angle in the case of a single tape spring [16, 31] or of integral slotted hinges [32] and nonlinear dynamic analyses were performed to capture the nonlinear phenomena (buckling, hysteresis, self-locking) characterising the deployment of tape springs in a planar motion [33, 34] and in a 3D-space [35].

Experimental tests, usually combined with finite element models used for the initial design or the correlation of the full deployment simulation, can be found in [23, 36] for single tape springs, in [17, 18, 37] for hinges composed of multiple tape springs, in [11, 32] for the deployment of integral slotted hinges and in [13] where tape springs are used as structural stiffeners for inflatable structures. The experimental data on the bending moment are collected in these works by the means of strain gauges without any correlated information on the configuration [36], or of load cells while the rotation angle is controlled and the motion kept planar [17, 37, 38]. Regarding displacements, the most common solution is to capture the motion with high-speed cameras and then post-treat the images [16, 18, 23, 32], which limits the experimental results to a 2D-space unless several cameras are used at the same time. Finally, in [10, 17], the dynamic tests had the particularity to be performed either on an air cushion table or during 0-g flights to approach microgravity conditions.

To the best of our knowledge, the accurate measurement of complete 3D motions and loads during deployment tests has not yet been achieved for the quantitative analysis of the structural response of tape springs and for the validation of detailed numerical models. In this work, an experimental set-up is then designed and submitted to deployment tests. To perform dynamic acquisitions, a 3D motion analysis system combined with a synchronised force plate are proposed. Furthermore, the experimental tests are repeated a large number of times in order to assess the reproducibility of the tape spring behaviour and of the measurements.

In parallel, a finite element model of the set-up is developed. To determine the inputs of the model, specific experimental tests are undertaken, in particular to evaluate the structural damping. A previous work [34] showed that this physical property is required to ensure a correct representation of the damping of the oscillations after deployment and of the self-locking phenomenon of the tape springs in their equilibrium state. Furthermore, it led to more robust simulations by reducing the sensitivity of the numerical models to the non-physical numerical dissipation of the transient solver. So far in the majority of the previously mentioned works, the dynamic simulations of tape springs were performed without any physical representation of the structural damping with only few notable exceptions that we could find: in [29, 30], it is represented by a diagonal damping matrix with constant damping elements chosen to fit directly the experimental deployment; in [11], the damping factors of the proportional damping model are functions of the natural frequency of the studied tape spring hinge; and in [27, 39], the parameters of a Prony series are fitted on the experimental evolution of the relaxation modulus of the tape springs at different temperatures.

In this work, it is then proposed to determine the structural damping which clearly affects the behaviour of tape springs by submitting the experimental set-up to a different kind of test consisting of small amplitude vibrations. The vibration decay allows completing and verifying the numerical results obtained in [34] where the structural damping was represented by a Kelvin-Voigt material model involving a single damping parameter. This simple model proved to be sufficient in [34] to capture the essential nonlinear dynamic phenomena encountered in the tape springs under study. The resulting finite element model representing the complete experimental set-up is then validated by comparing the numerical deployment tests to the experimental results.

The layout of this paper is as follows. The theoretical nonlinear behaviour of tape springs is explained in Section 2. The design of the experimental set-up and the acquisition equipment are described in Section 3. Then, in Section 4, experimental deployment tests and quasi-static tests are performed to gather information on the evolutions of the bending angle and the loads. In Section 5, the associated finite element model is defined and the required parameters are identified by the means of other experimental tests. The parameters are used to build a finite element model of the set-up which is compared to the experimental set-up in Section 6. Finally, the conclusions of this work are drawn in Section 7.

2 Theoretical nonlinear behaviour of tape springs

The advantageous characteristics of tape springs result from their highly nonlinear mechanical behaviour which is theoretically illustrated in Figure 4 and describes the evolution of the bending moment M determined at the clamped extremity of the tape spring when the bending angle θ is imposed at the other end.

First of all, the sense of bending has a significant impact on the behaviour and on the deformed configuration of the tape spring. The two senses of bending are defined as follows: the *opposite sense bending* ($M, \theta > 0$) leads to longitudinal and transverse curvatures in opposite sense, while the *equal sense bending* ($M, \theta < 0$) leads to longitudinal and transverse curvatures in the same sense [20].

In opposite sense, after first increasing linearly and reaching a maximum $M_{+}^{\max}$, the loading curve undergoes a sharp drop which is due to a buckling phenomenon caused by the formation of a symmetric fold in the middle of the tape spring. The fold

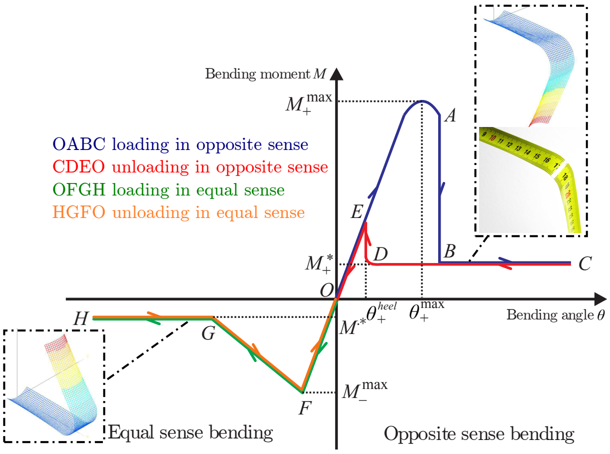

Figure 4: Theoretical evolution of the bending moment M with respect to the bending angle θ in pure bending (inspired from [16]).

curvature can be considered, as a first approximation, as equal to the transverse curvature of the non-deformed structure [24]. Once buckling occurred, larger rotation angles induce in theory no change in the bending moment which is defined as the residual moment M_+^*. During the unloading stage, the fold disappears for an angle θ_+^{heel} smaller than the one associated to buckling. This non-superposition of the loading and unloading paths is responsible for an hysteresis phenomenon which leads to a dissipation of energy and, in the end, to the self-locking of the structure in its deployed configuration.

On the other hand, the equal sense bending is also characterised by the formation of a transverse fold which results from the combination of torsion folds starting from the extremities and converging to the middle as the amplitude of the bending angle increases. This evolution being more progressive than in opposite sense, the maximum and residual moments are smaller in amplitude than their opposite sense counterparts ($|M_-^{max}| < M_+^{max}$, $|M_-^*| < M_+^*$). Finally, it is commonly accepted in theory that the cycles of loading-unloading are superimposed in equal sense bending even though it is not exactly the case in practice [23].

3 Description of the experimental set-up

The proposed experimental set-up is schematically illustrated in Figure 5. A dummy appendix is connected to the fixation support by two tape springs which are cut out from a common measuring tape. They have the same orientation so that the initial bending prior to deployment can be performed in opposite or equal sense by turning upside down the whole block composed of the tape springs, the interfaces, the rod and the dummy appendix. Furthermore, using two tape springs allows limiting the impact of torsion while keeping the structure as simple as possible [31]. Each extremity of the tape springs is clamped by interfaces composed of two complementary parts with curved regions fitting the geometry of the tape springs (Figure 5a).

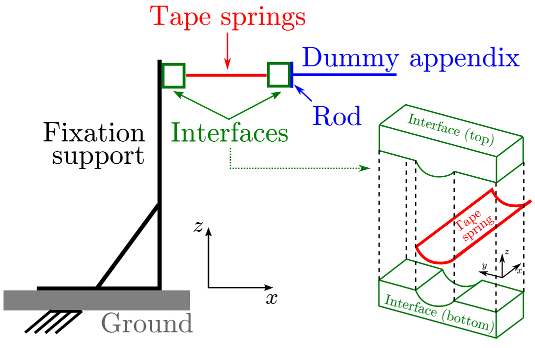

(a) Side view and interface.

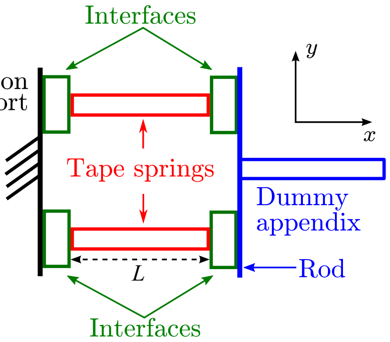

(b) Top view.

Figure 5: Schematic representation of the experimental set-up.

Table 1: Geometric characteristics of the tape springs used in the experimental set-up.

L [mm]	t [mm]	w [mm]	h [mm]	α [deg]	R [mm]
100	0.14	17.8	2.8	69.85	15.55

The geometric characteristics of the tape springs are given in Table 1 and illustrated in Figure 6. Only the length L, the thickness t, the width w and the height h were physically measured using a calliper, while the subtended angle α and the radius of curvature R were recovered with the help of simple trigonometric equations. Regarding the length L, it corresponds to the distance between the interfaces as illustrated in Figure 5b.

3.1 Determination of the maximum mass at the free end

One objective of this work is to study the folding and the autonomous deployment of the appendix de-

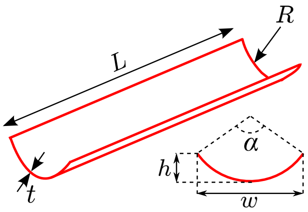

Figure 6: Geometric characteristics of tape springs.

spite the presence of the gravity field. It implies that, when designing the experimental set-up, one must ensure that the mass at the free end (the combination of two interfaces, the rod and the dummy appendix) is limited in order to respect two constraints. First of all, the structure cannot buckle under its own weight, and secondly, when initially folded downwards, the residual moment in the tape springs must be able to passively deploy the structure against gravity until the equilibrium state is recovered, whatever the initial sense of bending. As it can be deduced from the quasi-static relationship between the bending angle θ and the resulting bending moment M (Figure 4), the second constraint is the most restrictive one since $|M^*| < |M^{\max}|$. Furthermore, as explained previously, the amplitude of the residual moment is smaller in equal sense ($|M^*_-| < |M^*_+|$). It implies then that in order to use the same set-up in both senses, the maximum mass is constrained by the low value of the residual moment in equal sense bending.

The determination of this maximum mass is complicated by the existence of uncertainties affecting the values of the thickness t and the Young's modulus E of the tape springs. During the design phase of the experimental set-up, their impact was taken into account by performing parametric analyses. The detailed characterisation of the thickness t and the Young's modulus E is postponed to Section 5.1.

Based on a simple finite element model composed of two tape springs under gravity acceleration, the residual moment M^* can be evaluated at an angle of $\theta = 90°$. This angle is expected to be the initial bending angle in the experimental tests and, in that case, it is also the one which leads to the lowest value of the residual moment M^* as it either stays constant or slightly decreases after buckling. On the other hand, the moment due to gravity, which has to be counteracted, is the highest when the tape springs are close to their deployed configuration and is then equal to mgl. A passive deployment is then certainly possible if the following inequality is respected:

$$M^*(\theta = 90°) > mgl \tag{1}$$

where m is the mass, g is the gravity and l is the lever arm between the folds in the tape springs and the centre of mass of the mass. As a first estimation, the mass is considered as fixed at the tip of the tape springs and the folds are assumed to be located in the middle of the tape springs leading to $l = L/2$. The maximum masses respecting the inequality are then given in Figure 7 for the equal sense bending for different combinations of the thickness t and the Young's modulus E.

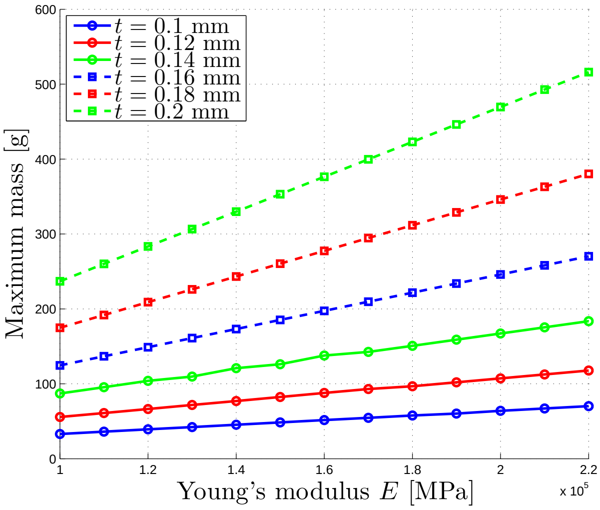

Figure 7: Maximum masses allowed for a passive deployment in equal sense bending.

As anticipated, the larger these parameters, the larger the allowed mass for a passive deployment. Furthermore, the residual moments and therefore the masses are proportional to t^3 for a fixed Young's modulus and linear with respect to E for a fixed thickness as expected from the simplified expressions of the residual moments [23]:

$$M^*_+ = (1+\nu)D\alpha \tag{2}$$
$$M^*_- = -(1-\nu)D\alpha \tag{3}$$

with the flexural rigidity $D = \frac{Et^3}{12(1-\nu^2)}$. For these parametric studies, instead of solving several finite element models, the simplified expressions of $M^*_\pm$ could have been exploited as a first approximation. However, compared to the finite element results, they lead to larger admissible masses by up to ~ 9 % in both senses, except for small thicknesses and Young's moduli in equal sense where decreases of up to 3.3 % are noticed. The use of finite element models was then preferred to improve the accuracy of the results and was automatised.

Starting from these values and iterating on the design of the set-up, the lever arm is re-evaluated and the mass is adjusted accordingly. In the end, the set-up described in the following section is obtained.

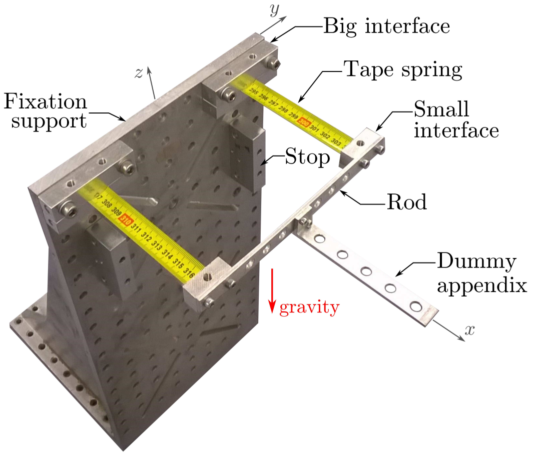

Figure 8: Experimental set-up.

3.2 Experimental set-up

The interfaces, the rod and the dummy appendix are designed to be as light as possible. This objective is achieved by drilling holes in the rod and the dummy appendix, while two types of interfaces are used. On the side of the fixation support, the interfaces are larger and thicker to ensure rigid links and an easy connection with the support. On the other side, to reduce the mass, the interfaces are clamped around the tape springs by the means of only one screw going through the tape springs. This resulting experimental set-up is visible in Figure 8 where the total mass at the free end reaches 77 g.

3.3 Acquisition equipment

In this work, the position of active markers fixed on the deployable structure is captured by the means of a 3D motion analysis system from CODAMOTION [40] (Figure 9). Each CX1 unit, located around the set-up, is able to triangulate the position of the markers as they combine three sensing arrays. Even though one unit would be sufficient, the four at our disposal are used to improve the accuracy which reaches 0.05 mm for the standard deviation in position along the longitudinal and vertical axes and 0.3 mm along the transversal axis when the distance between the markers and scanners is below 3 m. Furthermore, the acquisition frequency is fixed to 800 Hz and the real-time latency is below 10 ms.

To complete this system, a synchronised force plate from KISTLER (Type 9281E) [41] composed of four built-in piezoelectric sensors is located under the fixation support to collect information on the forces and the moments affecting the set-up during its deployment. The measuring ranges span from -125 N to 125 N along the three axes. The threshold is less than 250 mN, allowing thus accurate measurements even in the case of low loadings, while the acquisition frequency is 1 kHz.

This equipment is available in the Laboratory of Human Motion Analysis at the University of Liège [42].

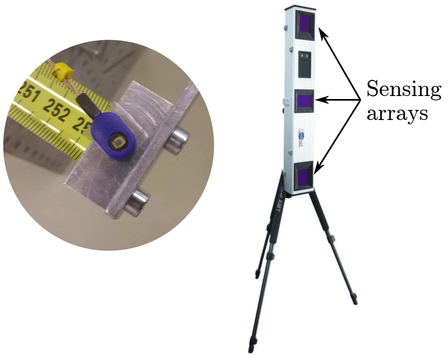

Figure 9: Marker and CX1 scanner from CODAMOTION [40].

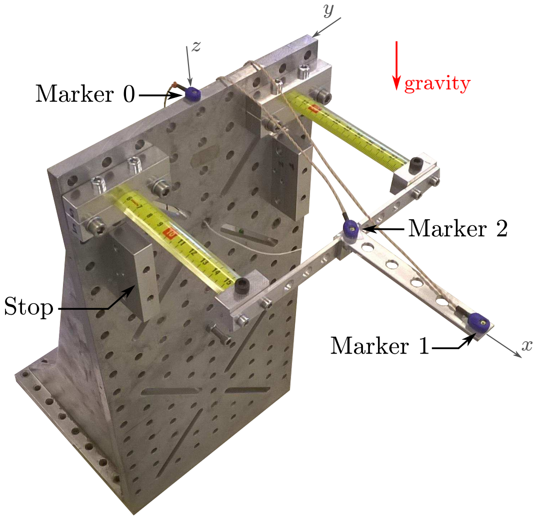

Figure 10: Deployed configuration of the experimental set-up in equal sense.

4 Experimental tests

The deployed configurations of the experimental set-up are given in Figures 8 and 10 for an initial folding in opposite and equal sense respectively. Compared to each other, the whole block composed of the four interfaces, the two tape springs, the rod and the dummy appendix is just turned upside down in order to start with a downwards initial folded configuration deploying against gravity in both cases.

The orientation of the y and z-axes is different according to the initial folded configuration in opposite (Figure 8) or equal sense (Figure 10). Thus, the experimental evolution of the bending angle measured positively about the y-axis respects the sign conven-

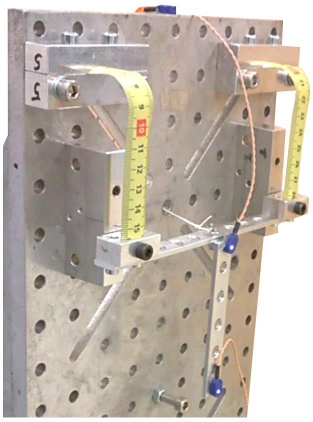

Figure 11: Initial folded configuration in equal sense of the experimental set-up.

tion defined in Section 2.

The experimental data are acquired with three markers located on the top of the fixation support, at the tip of the dummy appendix and in the middle of the rod. They are positioned in the symmetric plane of the set-up. The bending angle is then extracted from the relative positions of markers 1 and 2.

4.1 Deployment tests

The initial folded configuration is reached by pulling a rope attached in the middle of the rod until the small interfaces are in contact with stops attached to the fixation support (Figure 11). The initial folding leads thus to almost vertical deformed configurations which were assumed in the preliminary design of the set-up (Section 3.1). The mean initial bending angle reaches 95.5° and $-91.2°$ in opposite and equal sense respectively. The deployment is then triggered by cutting the rope which leaves the structure free to oscillate. For each sense of bending, two different pairs of tape springs are used to perform the deployment tests. The evolution of the bending angle with respect to the horizontal obtained in 50 tests are superimposed in Figures 12 and 14 for an initial folding in opposite and equal sense respectively. For the statistical analysis below, the data from 100 tests are exploited in each sense.

The evolution of the bending angle with an initial folding in opposite sense (Figure 12) can be divided into three phases depending on the types of fold created by the motion, the frequency of the oscillations and the amount of damping affecting each phase. The presence or the absence of folds is visually confirmed during the deployment. Relevant snapshots from the recorded videos are given in Figure 13 and can be linked to the evolution of the bend-

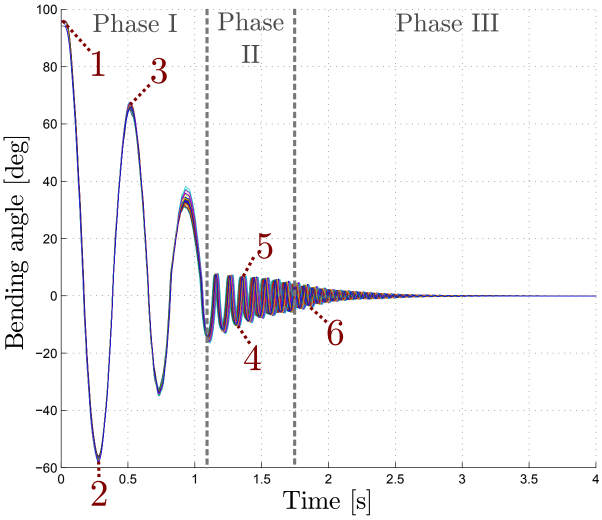

Figure 12: Experimental evolutions of the bending angle from the deployment tests in opposite sense.

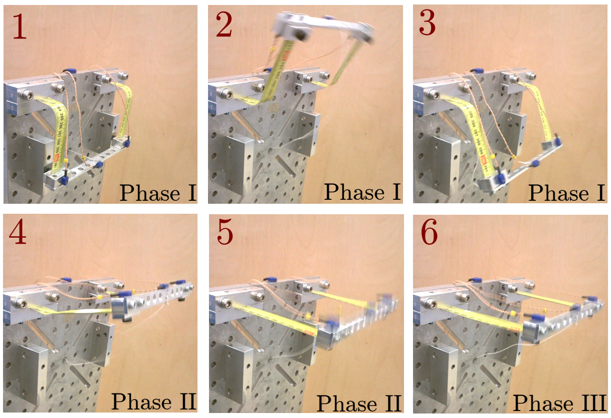

Figure 13: Deformed configuration of the experimental set-up in the different phases.

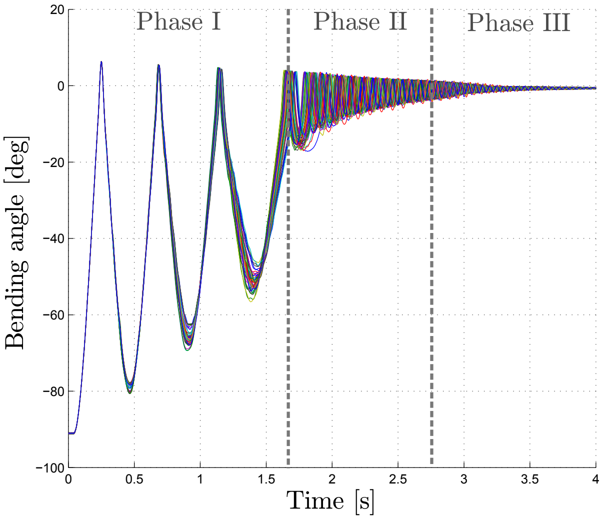

Figure 14: Experimental evolutions of the bending angle from the deployment tests in equal sense.

ing angle in Figure 12. In phase I, the energy in the structure is able to create folds in both senses of bending associated to large motion amplitudes occurring at a low frequency (Figure 13, snapshots 2 and 3). Since distinct nonlinear behaviours appear whether the fold is in opposite or equal sense, this evolution is asymmetric. The significant damping between each peak is mainly due to the hysteresis phenomenon described in Section 2. The relationship between the damping during the deployment and the hysteresis was investigated in [33]. Furthermore, as shown in [31], the quasi-static loading and unloading curves in equal sense are also not necessarily superimposed. It is then expected that during a dynamic deployment, this second hysteresis phenomenon is also responsible for some of the energy dissipation every time that a fold in equal sense disappears.

In phase II, folds are only formed in equal sense (Figure 13, snapshots 4 and 5), the remaining energy being not sufficient to reach and go beyond the maximum bending moment $M_+^{\max}$ in opposite sense which can often be twice as large as in equal sense $M_-^{\max}$. It implies that positive bending angles remain small and that shocks and rebounds occur at each positive peak. As in phase I, the evolution is then again asymmetric, but the frequency of oscillation increases as the system stays closer to the deployed configuration characterised by a higher stiffness. This time, the damping is caused by several phenomena: the hysteresis in equal sense, the shocks in opposite sense and the overall structural damping.

Finally in phase III, the tape springs vibrate without forming any folds as it can be seen by comparing the snapshots 4 and 6 in Figure 13. For small bending angles, a symmetric evolution of the motion is reached in which structural damping, drag effects and friction are predominant.

In the case of an initial folding in equal sense (Figure 14), in phase I, the initial stored elastic energy is too small to induce the formation of folds in opposite sense. The motion is then characterised by an asymmetric evolution at low frequency with folds in equal sense only. The same type of folds are present in phase II, but they occur at a higher frequency and lower amplitudes. The transition between phase I and phase II is due to the different deformation patterns of the tape springs. In the first case, the folds are well formed which leads to the complete transverse flattening of the tape springs, however, in the second case, the folds are only partially formed which leaves the tape springs with a certain curvature, increasing thus their stiffness. Finally, phase III is the same as the one in opposite sense without any formation of fold.

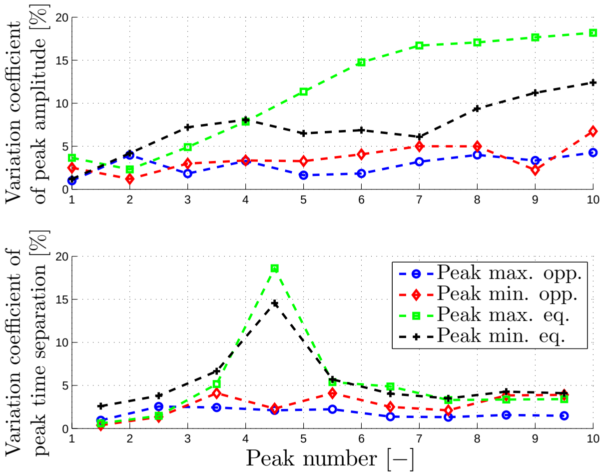

Figure 15: Variation coefficients of the first ten experimental peaks in amplitude and time separation of the bending angle for deployment tests.

In order to assess the reproducibility of the experimental results, the variation coefficients (or relative standard deviations) of the peak amplitude and the peak time separation are computed for the first ten maximum and minimum peaks in Figure 15. This variable is defined as the ratio between the standard deviation and the mean. Regarding the peak time separation, it corresponds to the elapsed time between each peak. The experimental tests show a good reproducibility for different tape springs and, as could be expected, the tests with an initial folding in equal sense are slightly less reproducible than the ones starting with a fold in opposite sense. It seems that the variability of these results is not dominated by the measurement uncertainties, but rather by the sensitivity of the mechanical response itself. Furthermore, the larger variation coefficients associated to the maximum amplitude peaks in equal sense are mostly due to their lower amplitudes, which are then more affected by small changes. Finally, the larger variation of the elapsed time between the peaks number 4 and 5 in equal sense is associated to the significant changes of amplitude between these peaks. This transition is then harder to capture than the rest of the bending angle evolution.

The deployments mainly remain in the xz-plane since the maximum lateral displacements reach amplitudes of 4.3 mm and 5.1 mm for initial foldings in opposite and equal sense respectively with respect to the equilibrium configuration. These values, measured at the tip of the appendix, correspond to 1.82 % and 2.18 % of the longitudinal length of the set-up, without including the fixation support.

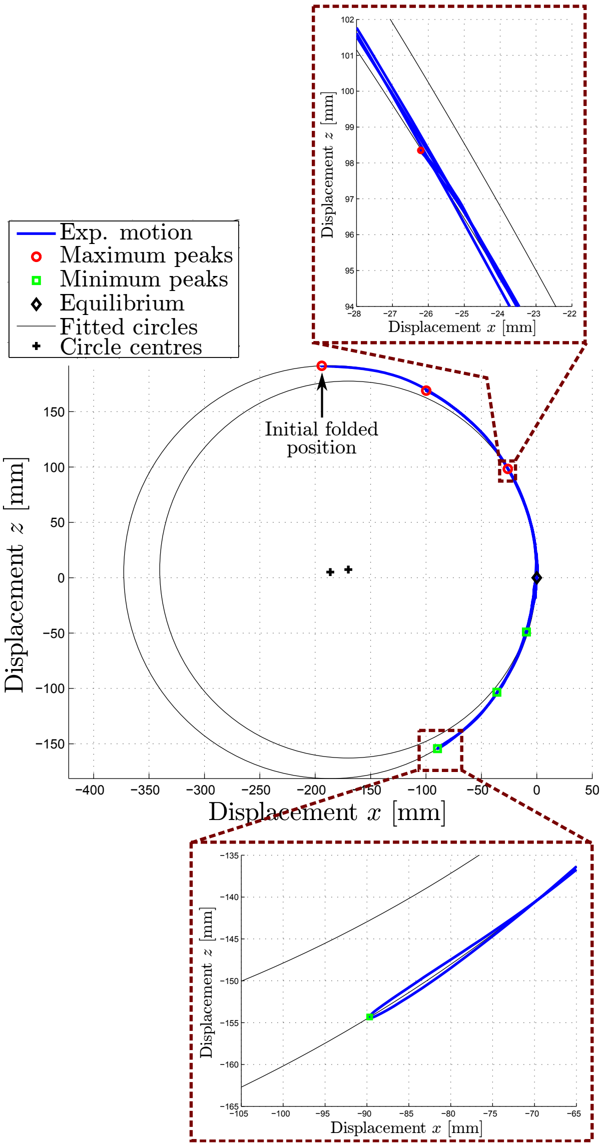

Figure 16: Experimental motion in the xz-plane of the appendix tip for an initial folding in opposite sense and fitted circles.

The trajectory of the appendix tip for a deployment with an initial folding in opposite sense in the xz-plane is illustrated in Figure 16 where the origin is centred on the equilibrium position. The other marked points on the experimental curve correspond to the maximum and minimum peaks visible in Figure 12 during phase I, including the initial folded position. It can be seen that the successive oscillations remain close to each other but are not perfectly superimposed and that, even though the trajectory looks circular at a first sight, it cannot be accurately captured by a single circular arc. Indeed, by fitting different sets of points, circles of different radii and centres are obtained. This behaviour can be explained by slight displacements of the folds along the tape springs.

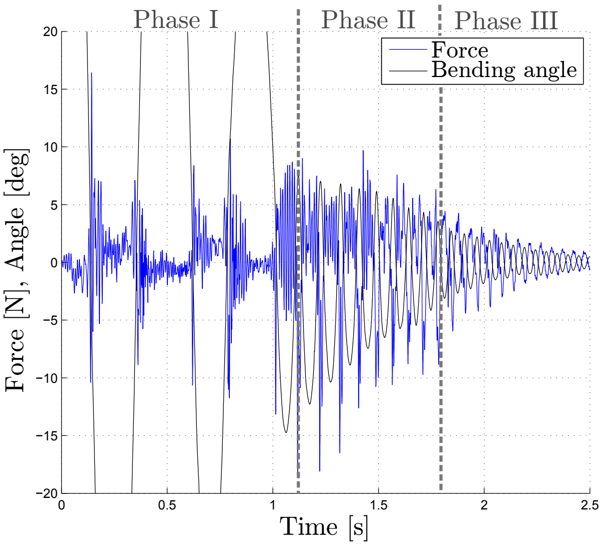

Figure 17: Experimental forces along the z-axis from the deployment tests with an initial folding in opposite sense, associated bending angle superimposed.

Regarding the vertical forces measured at the base of the fixation support by the means of the force plate, the three phases defining the evolution of the associated bending angle are clearly visible (Figures 17 and 18 for an initial folding in opposite and equal sense respectively). Each large peak occurs when the bending angle is close to zero and is thus linked to the formation and the disappearance of folds or to rebounds depending on the phase. In phase I, the peaks are well separated since the motion frequency is low, in phase II, the frequency increases as well as the occurence of folds in equal sense, finally in phase III, the absence of large force peaks is in accordance with the absence of folds.

The complexity of the force curves hinders the development of a quantitative reproducibility analysis. However, qualitatively, the presence of all the characteristic features in the measured forces mentioned previously was confirmed visually in each individual test.

4.2 Quasi-static tests

Quasi-static tests are performed on the experimental set-up without the dummy appendix in order to collect data on the maximum vertical force and the associated vertical displacement reached before the buckling of the tape springs. They consist in pulling vertically, by hand, on a string attached in the middle of the rod. They are performed as slow as possible and such that, in the end, the tape springs are folded in opposite sense.

One evolution of the vertical force obtained with these quasi-static tests is illustrated in Figure 19

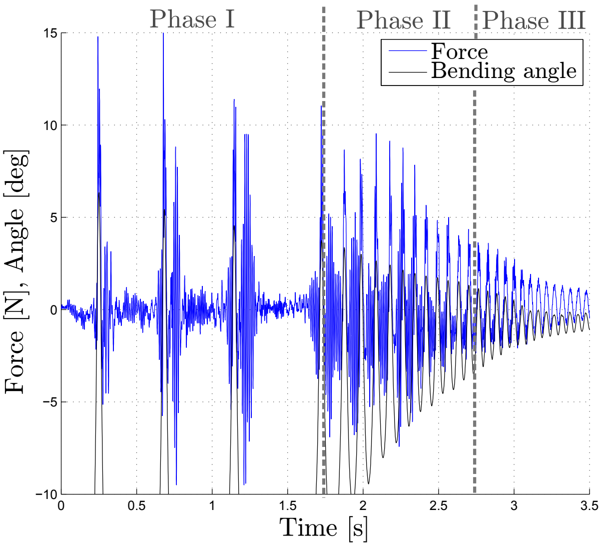

Figure 18: Experimental forces along the z-axis from the deployment tests with an initial folding in equal sense, associated bending angle superimposed.

where the vertical displacement is collected at marker 2 located in the middle of the rod. As it can be seen, the raw experimental data (full blue curve) is affected by noise which is due to the large measuring range of the force plate spanning from 0 to 125 N, while the measured force is below 11 N. The impact of the noise is then reduced by filtering with the `smooth` function from MATLAB [43] which consists of a moving average filter that replaces each value by a mean computed on the neighbouring data points defined within a span fixed here to 101 corresponding to an elapsed time of 25.3 ms. The resulting curve is the red dashed one used in the remaining of this section. Compared to the theoretical evolution of the bending moment with respect to the bending angle (Figure 4), the same characteristic features are visible: the load reaches a maximum, which is then followed by a sudden drop caused by the buckling of the tape springs.

To assess the reproducibility of the quasi-static tests, the value of the maximum force and of its associated displacement are compared on 50 curves obtained with two different pairs of tape springs. The results are summarised in Table 2 where three features are computed: the mean value, the maximum difference noticed between the results and the associated variation coefficient (or relative standard deviation). As the variation coefficients remain below 6 % in both cases, it can be concluded that these experimental tests show a good reproducibility, even though the motion was driven by hand.

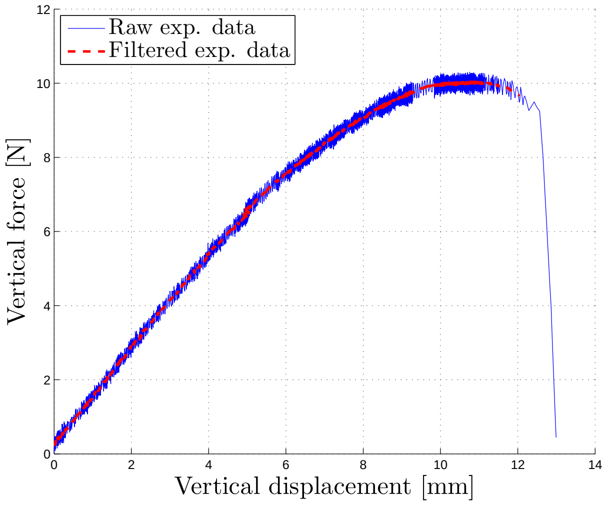

Figure 19: Experimental result of a quasi-static test.

Table 2: Experimental results from the quasi-static tests.

	Mean	Max. diff.	Variation coeff.
Force	9.8 N	1.3 N	3.33 %
Disp.	10.8 mm	4.6 mm	5.51 %

5 Finite element models

Finite element models are developed in order to reproduce and further investigate the deployment and quasi-static tests. Using the commercial software SAMCEF [44], the general model of the experimental set-up illustrated in Figure 20 is defined.

The modelling assumptions are the following:

- the tape springs, the rod and the dummy appendix are represented by flexible Mindlin shells characterised by a uniform isotropic material;
- the tape springs, which in reality are multi-layered composites, are simplified as single-

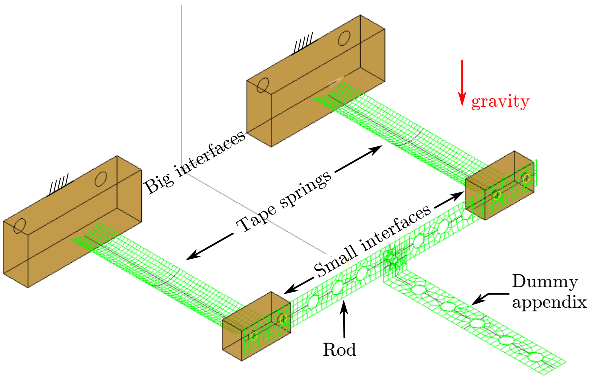

Figure 20: General finite element model of the experimental set-up.

layered elements with equivalent thickness and Young's modulus (see Section 5.1 for detailed developments). They are assumed to be characterised by uniform geometric parameters;

- the global structural damping of the whole structure is represented by a single equivalent parameter introduced in the Kelvin-Voigt material model of the tape springs (see Section 5.2 for detailed developments). Drag effects due to air resistance are included in that parameter as their contribution cannot be precisely separated from the other damping phenomena in the present experiments;
- based on convergence analyses with respect to the mesh size, it is set to 2 mm for the tape springs to accurately capture the large deformations and the nonlinear phenomena, while it is fixed to 3 mm for the rod and the dummy appendix which are expected to be weakly deformed;
- the four interfaces and their fixation screws are represented by rigid volumes;
- the connexions at the interfaces and between the rod and the dummy appendix are considered as rigid;
- the fixation support is not included in the model, implying thus that the structure is assumed to be clamped at the big interfaces;
- gravity is represented by a global acceleration along the vertical axis applied on the whole model;
- deployment tests, equivalent to the experimental ones described in Section 4.1, are divided in three phases: starting from the deployed configuration, the structure is folded by forcing the node representing marker 2 in Figure 10 to reach its initial position measured experimentally. This phase is performed at a displacement rate of less than 2 mm/s in order to have a quasi-static folding. Then the structure is stabilised in its folded configuration during 5 s. Finally, the deployment is triggered by removing the displacement constraint on marker 2;
- quasi-static tests, equivalent to the experimental ones described in Section 4.2, are performed by controlling the vertical displacement of the middle of the rod. A displacement rate of 1 mm/s is imposed until buckling occurs.

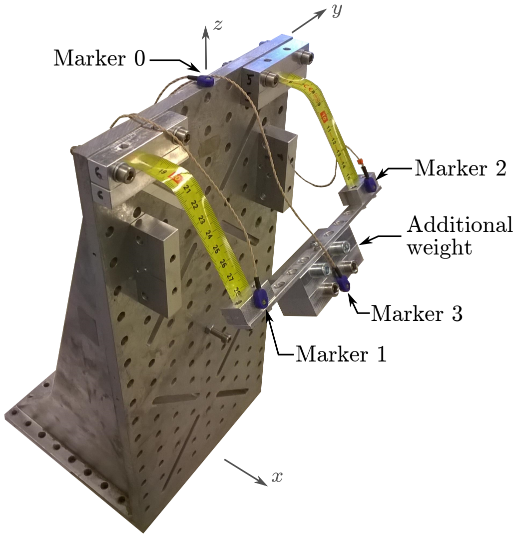

Figure 21: Deformed configuration of the experimental set-up used to determine equivalent values of the thickness and the Young's modulus.

Regarding the solver, the second-order accurate generalised-α method is used [45]. The evolution of the time steps is adaptive in order to capture the nonlinear phenomena with precision and to reduce the simulation time otherwise. Finally, the numerical damping, defined as the spectral radius at infinite frequencies ρ_∞, is chosen so that its impact on the results is limited, but still allows the solver to converge (see Section 5.2 for detailed developments). It ranges from 0 to 1, 0 meaning a complete annihilation of the high-frequency content and 1 meaning no numerical dissipation.

Identification methods are then required to determine the three uncertain parameters: the thickness, the Young's modulus and the structural damping. These issues are addressed in the following sections.

5.1 Identification of the thickness and Young's modulus

Experimental tests The thickness and the Young's modulus are identified based on a configuration of the set-up with two static equilibria: a folded one and an unfolded one. For that purpose, an additional weight is fixed to the rod so that, after buckling, the residual moment does not trigger a passive deployment and a new static folded equilibrium configuration exists (Figure 21). The measured displacements for the two equilibrium configurations are then used to determine the equivalent thickness and Young's modulus.

The data acquisition is performed with four active markers which are placed on the set-up as follows.

Table 3: Displacements in absolute values of the markers to reach the deformed configuration used to determine equivalent values of the thickness and the Young's modulus.

	|Displacement| [mm]		
	x	y	z
Marker 0	0.2	0.1	0.1
Markers $1-2$	24.7	0.1	77.9
Marker 3	41.8	0.6	110.9

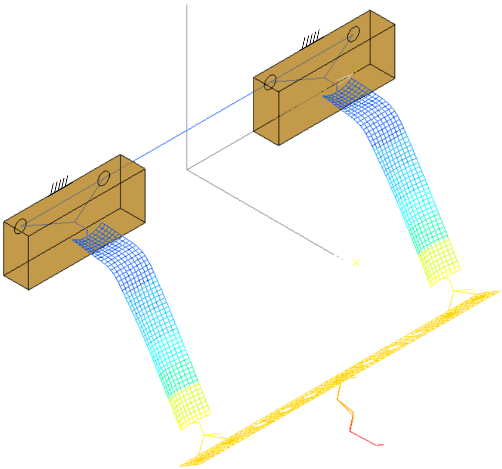

Figure 22: Finite element model used to determine equivalent values of the thickness and the Young's modulus (deformed configuration).

Marker 0 is located on the fixation support and is used as a control point as it remains fixed. Displacements measured at markers 1 and 2 on the small interfaces are used to obtain average values at both locations as in theory they should be equal. However, experimentally, some differences might be encountered, for example due to the set-up not being perfectly symmetric or perfectly aligned along the axes. Finally, a last marker is located at the tip of the additional weight. The measured displacements, in absolute values, are given in Table 3.

Finite element models To determine the equivalent values of the Young's modulus E and the thickness t, a model reproducing the deformed configuration after the formation of the folds is developed.

In this case, the simulation follows two steps: first, the displacement at the tip of the additional weight, considered as rigid, is imposed in order to force buckling, then that displacement constraint is removed and the structure stabilises in the sought deformed configuration given in Figure 22.

Table 4: Lower and upper bounds of the design variables in the optimisation procedure.

Bounds	E [MPa]	t [mm]
min	100000	0.12
max	220000	0.2

Table 5: Results of the optimisation procedure.

E [MPa]	t [mm]
151760	0.138

Optimisation procedure The Young's modulus E and the thickness t fitting at best the previous experimental results are obtained by solving an optimisation problem expressed as:

$$\min_{E,t} f(E,t) \text{ such that } \left\{ \begin{array}{c} E_{\min} \leq E \leq E_{\max} \\ t_{\min} \leq t \leq t_{\max} \end{array} \right. \tag{4}$$

where $f(E,t)$ is the objective function to be minimised and quantifies the correlation between the numerical and the mean experimental results. To this end, displacements along the x and z-axes are compared, while the displacements along the y-axis are not included in the optimisation problem. The objective function $f(E,t)$ is then the sum of the differences in absolute values, each term being divided by the corresponding mean experimental value in order to sum adimensional terms with the same order of magnitude.

Regarding the bounds limiting the design variables, the ranges of values allowing a passive deployment of the mass and which are based on the developments in Section 3 are used (Table 4).

The problem is solved by the means of the interior-point algorithm available through the `fmincon` function in MATLAB which solves large, sparse multivariable problems, as well as small dense ones [43]. This method aims at finding a local minimum of the objective function, which may depend on the initial guess. Therefore, several tests starting at different points of the ranges in Table 4 are performed before finding a global solution.

The final results of the optimisation procedure are given in Table 5, while the comparison of the displacements obtained experimentally and numerically is computed in Table 6. Thanks to this latter, it can be concluded that it is reasonable to model each tape spring as an homogeneous structure with an equivalent thickness and an equivalent Young's modulus.

In order to fully define the isotropic material, the Poisson's ratio has to be determined in addition to

Table 6: Comparison between the results of the experimental tests and the optimisation procedure.

		|Displacement|		
		Exp. [mm]	Num. [mm]	Δ [%]
M. $1-2$	x	24.7	25.7	4.1
	z	77.9	77.9	<0.1
M. 3	x	41.8	43.7	4.6
	z	110.9	111.6	0.6

the Young's modulus. By performing optimisation procedures in which the Poisson's ratio is also a design variable, it was found that both parameters have a similar impact on the tape spring behaviour. The same quasi-static and dynamic responses could then be obtained whether the Poisson's ratio was left free to vary or not. It was then decided, as it was done in this section, to fix the Poisson's ratio *a priori* to a value of 0.3 in order to reduce the number of design variables.

5.2 Identification of the structural damping

The next physical feature to determine is the structural damping of the Kelvin-Voigt material model. This rheological model is defined by a stiffness identified in the previous section and a viscosity coefficient η acting in parallel and leads to the exponential decay of vibratory motions [46].

In the case of tape springs, the structural damping ε is required to capture the damping of the small amplitude oscillations after deployment and the self-locking in the deployed state [34]. Furthermore, it only affects the physically-relevant low frequency response of a model. In contrast, the numerical damping is used to filter the high frequency modes poorly represented in the discretised finite element models and is needed to ensure the convergence of the solver.

The structural damping is a physical property of the material composing the tape springs. However, additional sources of damping are present in the experimental set-up due to the dissipation at the connections between each element, the flexibility of other components which are also characterised by a certain amount of structural damping, the air resistance as the tests are not performed in vacuum or the acoustic effects which can be heard when a fold is formed or disappears. Thus, the structural damping of the tape springs cannot be easily isolated in this case from all the other sources of dissipation and the experimental measurements performed here give only a global information on the dissipation phenomena in the whole structure.

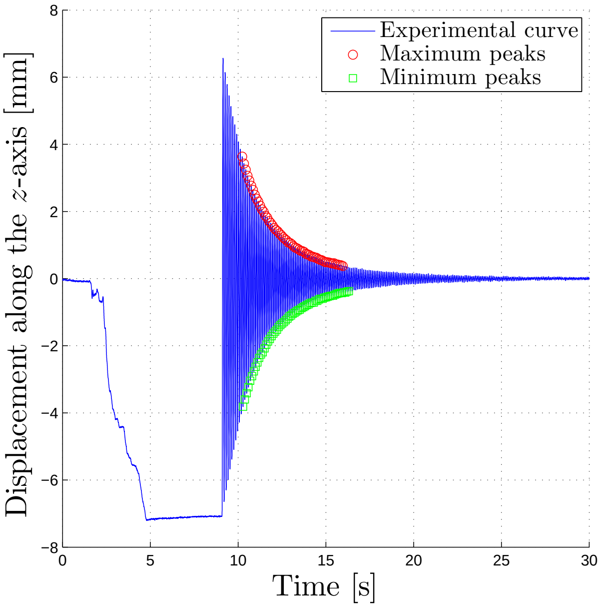

Figure 23: Experimental result of one small amplitude vibration test.

Experimental tests In order to evaluate the value of the viscosity coefficient η, the experimental set-up is submitted to small amplitude free vibrations at its free end. The displacements of the extremity are limited to small values to ensure that during the tests no fold is formed in the tape springs and their behaviour remains in the quasi-linear part described in Figure 4. Thus, it focuses on the phase III described in Section 4.1. As for the identification of the thickness and the Young's modulus, the dummy appendix is replaced by an additional weight (Figure 21) in order to reduce the frequency of these vibrations and improve the accuracy of the collected data.

Experimentally, the tests are performed with an initial vertical displacement around 8 mm reached by applying, manually, a vertical load on the additional weight, nevertheless, only the peaks belonging to the intervals $\pm[0.4;4]$ mm are exploited. Indeed, displacements larger than 4 mm are too close to buckling and it cannot be assumed that the behaviour of the tape springs is still linear, while for displacements smaller than 0.4 mm, the experimental data are too altered by noise. One result of the small amplitude vibration tests is illustrated in Figure 23 in terms of displacements around the equilibrium configuration. It can be seen that the response is dominated by a single oscillation frequency and that the damping of the oscillations tends to follow an exponential decay.

Assuming that the system behaves as a damped

Table 7: Experimental results from the small amplitude vibration tests with ε the structural damping and Δt the oscillation period.

	Mean	Max. diff.	Variation coeff.
ε	0.509 %	0.288 %	20.67 %
Δt	0.100 s	0.003 s	0.919 %

single degree of freedom harmonic oscillator:

$$\ddot{z} + 2\varepsilon\omega_0\dot{z} + \omega_0^2 z = 0 \tag{5}$$

the values of the natural pulsation ω_0 and the structural damping ε are fitted based on the peaks respecting the ranges previously mentioned and highlighted in Figure 23.

In total, 510 small amplitude vibration tests were performed on 4 different pairs of tape springs during 11 sessions of tests. After each session, mean values were determined for both the structural damping ε and the oscillation period Δt, this latter being used to solve the relationship:

$$\Delta t = \frac{2\pi}{\omega_0\sqrt{1-\varepsilon^2}} \tag{6}$$

For information, it was not always possible to perform the same number of tests per session. The general mean on all the sessions is given in Table 7, along with the maximum difference noticed between sessions and the associated variation coefficient (or relative standard deviation).

It can be concluded from Table 7 that the experimental measurement of the structural damping ε is quite sensitive, its value experiencing significant changes from one session of tests to another. Several elements were identified to explain this lack of robustness. First of all, the structural damping is sensitive to the assembly of the set-up. Indeed, between sessions, disassembling and re-building the set-up with the same tape springs led to variations in the mean structural damping. Furthermore, changing the tape springs also impacts that parameter since the measuring tape from which they are cut out is probably not perfectly uniform. Finally, within a session of tests, the value of the structural damping tends to decrease as the number of tests increases as it can be seen in Figure 24. This behaviour is not clearly understood but is most likely due to thermal effects and unmodelled material phenomena.

Regarding the oscillation period Δt, this parameter is much less sensitive to all the disruptive elements mentioned previously and remains fairly stable between each session of tests.

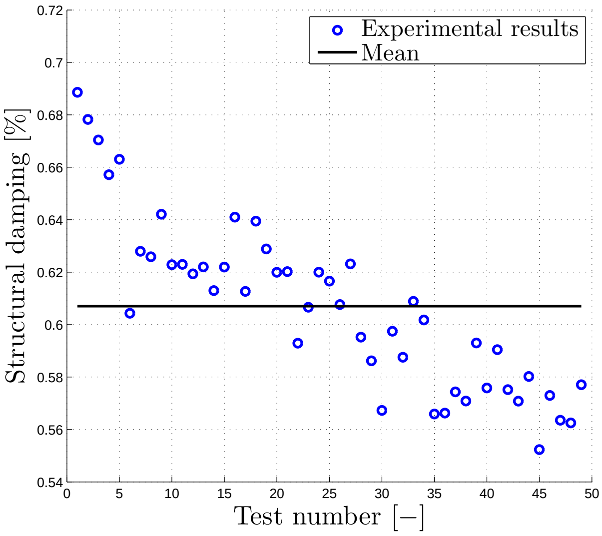

Figure 24: Evolution of the structural damping ε during the third session of small amplitude vibration tests.

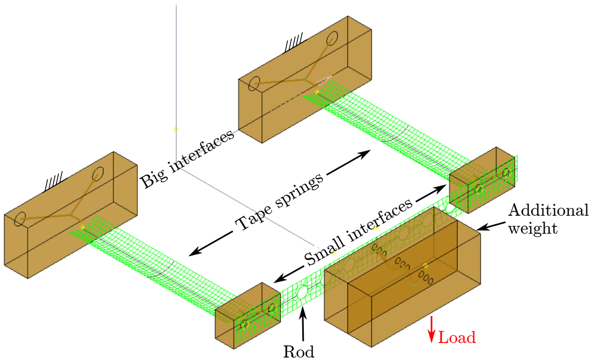

Figure 25: Finite element model used for the small amplitude vibration tests.

Finite element model Numerically, the small amplitude vibration tests are performed on the finite element model illustrated in Figure 25. As it was done experimentally, a vertical load is applied on the additional weight to reach the initial vertical displacement, then the structure is left free to oscillate.

The solver used in this case is the generalised-α method [45]. In order to determine the most appropriate value of numerical damping ρ_∞ which has a limited impact on the results, but still allows the convergence of the solver and a reasonable computation time, a parametric study is performed. In Figure 26, it can be seen that, as it was already shown in [34], an excessive increase of the amount of numerical damping (corresponding to a reduction of the value of ρ_∞) has a significant impact on the results of the small amplitude vibration tests, especially the structural damping. On the other hand, large values of ρ_∞ lead to larger computation time. In the following simulations, the value of the numerical damping ρ_∞

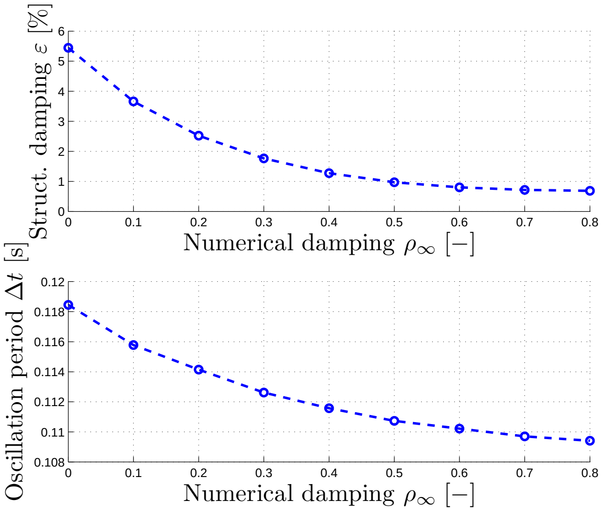

Figure 26: Impact of the numerical damping ρ_∞ on the structural damping ε and the oscillation period Δt.

Table 8: Experimental and numerical results from the small amplitude vibration tests.

	Exp.	Num.	Δ
ε	0.509 %	0.505 %	0.79 %
Δt	0.100 s	0.110 s	10 %
η	–	$1.73e^{-4}$ s	–

is then set to 0.7 which appears as a reasonable compromise.

For a single degree of freedom system, the viscosity parameter η of the Kelvin-Voigt model is linearly related to the structural damping ε as:

$$\varepsilon = \frac{\eta}{2\omega_0 m} \tag{7}$$

where m is the mass. In the case of the finite element model in Figure 25, the linearity of the relationship is preserved under the small vibrations condition and the value of η can be adjusted to fit the exponential decay observed experimentally. For that purpose, the values of ε and Δt were extracted from the numerical results using the same procedure developed to post-treat the experimental results.

The final numerical results are given in Table 8 and compared to the experimental ones. It can be seen that there is a good agreement in the structural damping ε, but a bigger difference in the oscillation period Δt. This last observation can be explained by the fact that the oscillation period Δt mostly depends on the Young's modulus and the thickness of the tape springs, which were here identified from static tests (Section 5.1).

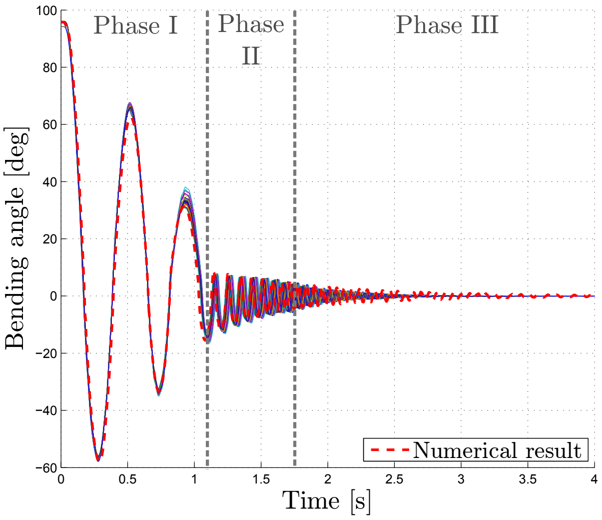

Figure 27: Qualitative comparison between the experimental and the numerical bending angles during the deployment tests in opposite sense.

6 Comparison between the experimental and numerical results

After the identification of all the parameters required to build the finite element models based on static and linear vibration tests, the deployment and quasi-static tests respectively described in Sections 4.1 and 4.2 can be simulated. At this level, no further calibration of the model was performed, *i.e.* the simulations are performed in a purely predictive manner.

6.1 Deployment tests

Regarding deployment tests starting with an initial folding in opposite sense, the finite element model is able to correctly capture the three phases characterising the evolution of the bending angle as it can be seen in Figure 27 where the numerical simulation is superimposed on experimental results. The main discrepancy is an underestimation of the damping in phase III. In order to compare these results quantitatively, the difference, in absolute value, between the first ten maximum and minimum peaks in terms of amplitude and time separation is computed (Figure 28). It can be seen that the differences mainly remain below 1.5° throughout the simulation without significant variation, except for the first maximum peak occurring around 0.5 s. It can be concluded from this comparison that the behaviour of the finite element model deploying with an initial bending in opposite sense is validated.

In the case of an initial folding in equal sense (Figure 29), it can be seen that the finite element model is characterised by less damping than the experimental

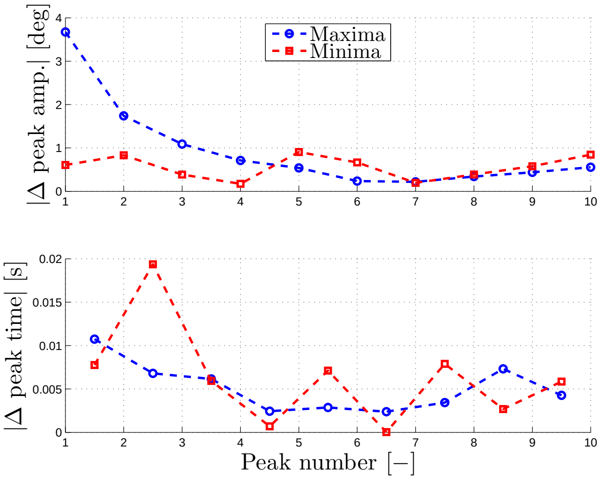

Figure 28: Quantitative comparison between the experimental and the numerical peak amplitude and peak time separation during the deployment tests in opposite sense.

set-up, which results in an additional large amplitude peak around 2 s. Nonetheless, if that fourth peak is left aside, the quantitative comparison (Figure 30) shows that, in terms of amplitude, the main differences are encountered at the first three minimum peaks which are due to the underestimation of the damping. For the other minimum and all the maximum peaks, the differences remain stable and below 1.5°, as in the opposite sense case. Regarding the peak time separation, if the fourth peak is again discarded, it can be seen that the model is slightly less accurate for deployments in equal sense than in opposite sense.

Further investigations of the experimental set-up have shown that the motion triggered by an initial folding in equal sense is sensitive to the initial conditions. For example, it is possible to recover a fourth large amplitude peak experimentally by changing the layout of the marker cables visible in Figure 10. The resulting evolution of the bending angle is given in Figure 31 with the associated numerical result. The finite element model shows a similar sensitivity. Indeed, by increasing the value of the damping parameter in the Kelvin-Voigt model to $2.1e^{-4}$ s, it is possible to remove the fourth large amplitude peak (Figure 32).

Regarding the vertical forces that are experimentally measured at the base of the fixation support (Figure 33, blue curve) and that are numerically measured at the clamped interface (Figure 33, red curve), disparities appear in terms of amplitude, but most importantly the high frequency vibrations of small amplitude separating the experimental peaks are not captured numerically. However, by adding

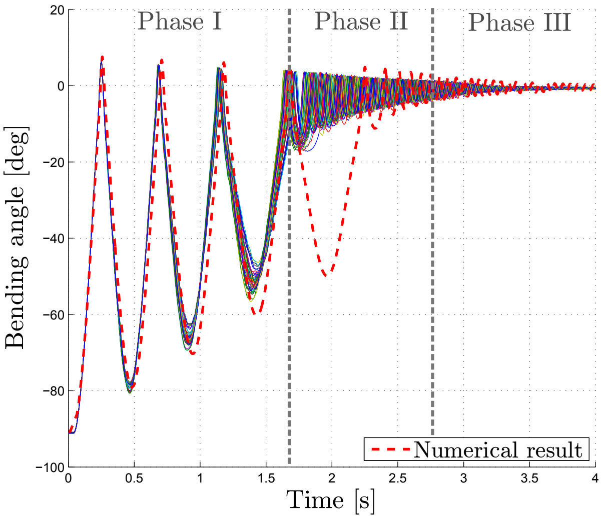

Figure 29: Qualitative comparison between the experimental and the numerical bending angles during the deployment tests in equal sense.

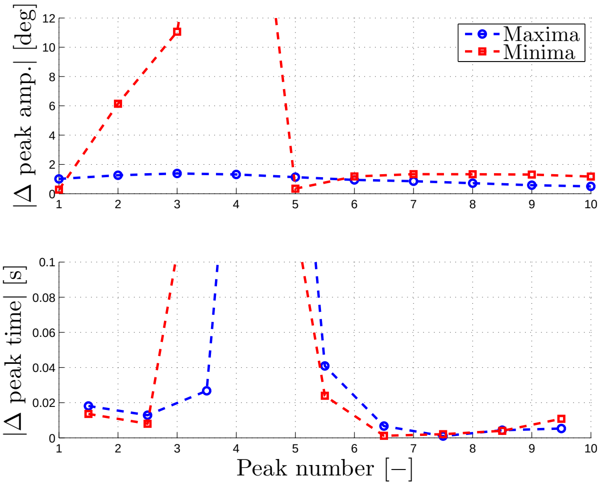

Figure 30: Quantitative comparison between the experimental and the numerical peak amplitude and peak time separation during the deployment tests in equal sense.

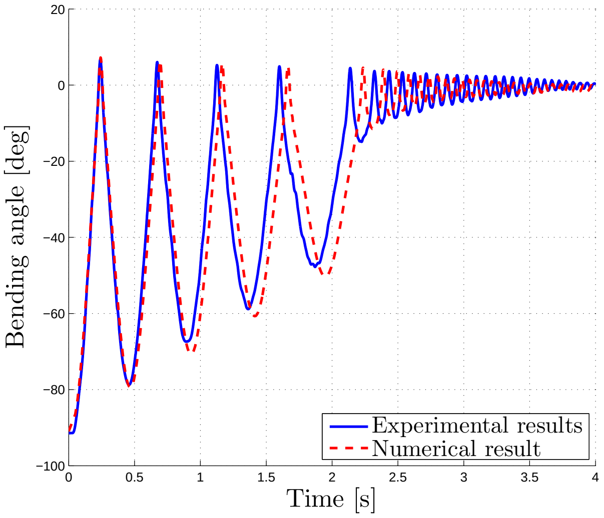

Figure 31: Deployment tests in equal sense: slightly disturbed experimental set-up.

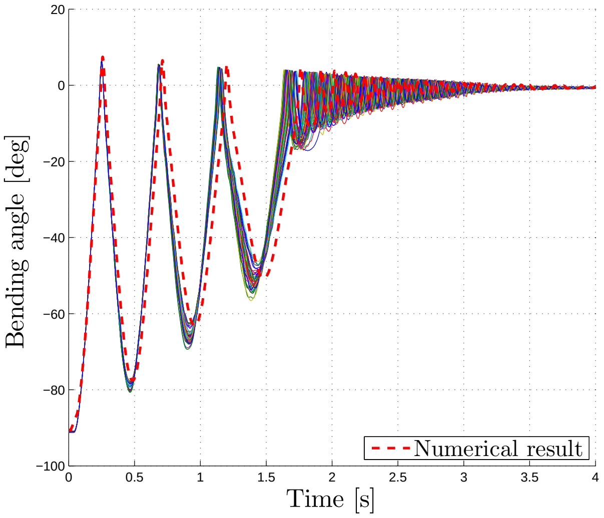

Figure 32: Deployment tests in equal sense: slightly disturbed finite element model.

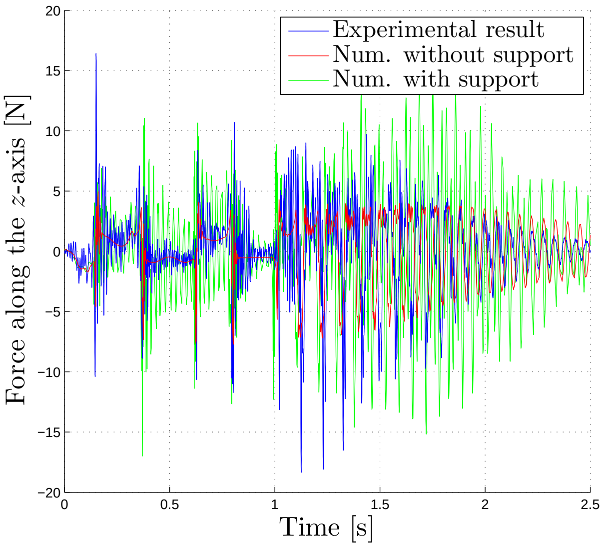

Figure 33: Qualitative comparison between the experimental and the numerical vertical forces during the deployment tests.

Table 9: Comparison between the mean experimental and numerical results of the quasi-static tests.

	Exp.	Num.	Δ [%]
Max. load [N]	9.8	7.6	22.4
Disp. [mm]	10.8	10.1	6.48

a flexible model of the support using a shell finite element mesh, the high frequency vibrations are recovered (Figure 33, green curve), but their amplitudes are overestimated and require more time to be damped out. A more detailed investigation of the flexibility of the support could be done in the future in order to better match the forces observed in the simulations and in the experiments. Alternatively, a stiffer support structure could be designed to reduce the influence of the flexibility.

6.2 Quasi-static tests

A comparison between the experimental and numerical quasi-static tests shows noticeable differences in terms of maximum vertical force before buckling (Table 9). Nonetheless, the associated vertical displacement is fairly captured. This evolution is confirmed qualitatively in Figure 34 where one experimental and the numerical results are superimposed, along with the lowest and highest experimental curves. This difference in forces can be attributed to our assumption to represent multi layered tape springs by single layered elements.

The fact that the pre-buckling behaviour from quasi-static tests is captured with less accuracy seems to be due to the current identification ap-

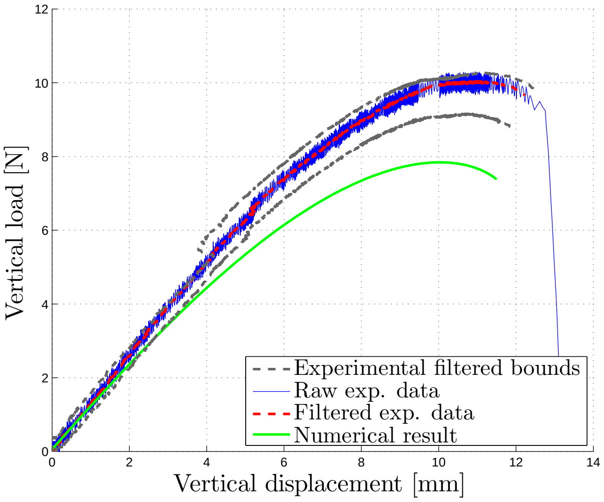

Figure 34: Comparison between one experimental quasi-static test and the numerical model.

proach which focuses on the post-buckling response. Indeed, the thickness and the Young's modulus used in the model were identified by comparing an equilibrium configuration of the set-up obtained after buckling to the underformed state. Furthermore, the hypothesis that the material and the geometry, especially the thickness and the transverse curvature, are uniform along the tape springs could also explain these differences between the experimental and numerical results since, in practice, these parameters are most likely not uniform and have a great influence on the quasi-static behaviour of tape springs as shown in [16, 31].

7 Conclusions

The experimental set-up designed in this work is used to analyse the nonlinear behaviour of compliant mechanisms called tape springs. Their geometric nonlinearity is responsible for complex phenomena such as buckling, the formation of folds and hysteresis.

The experimental data are collected by the means of a 3D motion analysis system combined with a synchronised force plate. The post-processing of deployment tests shows that the evolution of the motion can be divided in three phases defined by different types of folds, frequencies of oscillation and damping behaviours, their characteristics being influenced by the initial sense of folding of the tape springs. These phases are also clearly visible in the evolution of the experimental loads affecting the structure. Nonetheless, this complex dynamic evolution remains mainly planar and shows a good reproducibility, especially for opposite sense motions.

To further investigate the structural behaviour, finite element models are developed. Based on simple experimental tests, the required parameters are identified: by comparing two static equilibrium configurations of the set-up, the thickness and the Young's modulus of the tape springs are determined, while small amplitude vibration tests are performed to collect data on the structural damping. Regarding this latter, the experimental tests show that its value is subject to a high variability which is attributed to the assembly of the set-up, the non-uniformity of the tape springs, thermal effects and unmodelled material phenomena. Nonetheless, a simple material law defined by the Kelvin-Voigt model is sufficient to capture the essential nonlinear dynamic behaviours observed in the present tests.

For deployment tests with an initial folding in opposite sense, a good correlation between the experimental and numerical results is obtained. In the equal sense case, both the experimental set-up and the finite element model prove to be particularly sensitive to the initial conditions and the system parameters. Finally, the transmitted forces experimentally measured at the base of the support are influenced by the flexibility of the support model.

In future works, the same identification and validation procedures could be used in 3D experiments with more significant out-of-plane motions. Furthermore, the set-up could be exploited to further improve the finite element model by analysing in detail the sensitivity of the tape spring behaviour in equal sense, dedicating specific tests to the evolution of the forces affecting the structure and also exploiting more complex structural damping models.

Acknowledgements

The authors would like to thank Prof. Davide Ruffoni and Ir. Laura Zorzetto from the Mechanics of Biological and Bio-inspired Materials Research Unit (University of Liège, Belgium) for their technical help in the development of static experimental tests.

The first author would like to acknowledge the Belgian National Fund for Scientific Research for its financial support.

References

[1] L.L. Howell, Compliant Mechanisms, *John Wiley & Sons, New York*, 2001.

[2] K.A. Tolman, E.G. Merriam, L.L. Howell, Compliant constant-force linear-motion mech-

anism, *Mechanism and Machine Theory* **106**, 2016, 68–79.

[3] J.C. Meaders, C.A. Mattson, Optimization of near-constant force spring subject to mating uncertainty, *Struct. Multidisc. Optim.* **41**, 2010, 1–15.

[4] S. Hussain, S.Q. Xie, P.K. Jamwal, J. Parsons, An intrinsically compliant robotic orthosis for treadmill training, *Medical Engineering & Physics* **34**, 2012, 1448–1453.

[5] K.J. Lu, S. Kota, Design of compliant mechanisms for morphing structural shapes, *Journal of Intelligent Material Systems and Structures* **14**, 2003, 379–391.

[6] C. Kim, et al., Design of an auto-focusing actuator with a flexure-based compliant mechanism for mobile imaging devices, *Microsyst. Technol.* **19**, 2013, 1633–1644.

[7] G. Binnig, C.F. Quate, C. Gerber, Atomic Force Microscope, *Phys. Rev. Lett.* **56 (9)**, 1986, 930–933.

[8] S. Pellegrino, Deployable Structures in Engineering, *Deployable Structures*, CISM Courses and Lectures, vol. 412, Springer (Wien), 2001.

[9] O. Sigmund, On the design of compliant mechanisms using topology optimization, *Mechan. Struct. Mach.* **25 (4)**, 1997, 493–524.

[10] J. Sicre, D. Givois, E. Emerit, Application of Maeva hinge to Myriade microsatellites deployments needs, in: *11th European Space Mechanisms and Tribology Symposium (ESMATS) 2005, ESA/CNES*, Lucerne, Suisse, 21–23 September 2005.

[11] M. Mobrem, D. Adams, Deployment analysis of lenticular jointed antennas onboard the mars express spacecraft, *J. Spacecr. and Rockets* **46**, 2009, 394–402.

[12] J.T. Black, J.A. Whetzal, B.J. deBlonk, J.J. Massarello, Deployment repeatability testing of composite tape springs for space optics applications, in: *Proceedings of the 47th AIAA/ASME/ASCE/AHS/ASC Structures, Structural Dynamics, and Materials Conference*, Newport, Rhode Island, USA, 1–4 May 2006.

[13] A.J. Cook, S.J.I. Walker, Experimental research on tape spring supported space inflatable structures, *Acta Astronaut.* **118**, 2016, 316–328.

[14] L. Johnson, M. Whorton, A. Heaton, R. Pinson, G. Laue, C. Adams, NanoSail-D: A solar sail demonstration mission, *Acta Astronaut.* **68**, 2011, 571–575.

[15] C. Sickinger, L. Herbeck, Deployment strategies, analyses and tests for the CFRP booms of a solar sail, in: *Proceedings of the European Conference on Spacecraft Structures, Materials & Mechanical Testing*, Toulouse, France, 11–13 December 2002

[16] K.A. Seffen, S. Pellegrino, Deployment of a rigid panel by tape-springs, *Department of Engineering, University of Cambridge, Report CUED/D-STRUCT/TR168.*, 1997.

[17] D. Givois, J. Sicre, T. Mazoyer, A low cost hinge for appendices deployment: design, test and application, in: *9th European Space Mechanisms and Tribology Symposium*, Liège, Belgium, 19-21 September 2001.

[18] C. Boesch, et al., Ultra light self-motorized mechanism for deployment of light weight space craft appendages, in: *39th Aerospace Mechanisms Symposium*, NASA Marshall Space Flight Center, 7-9 May 2008.

[19] H.M.Y.C. Mallikarachchi, S. Pellegrino, Quasi-static folding and deployment of ultrathin composite tape-spring hinges, *J. Spacecr. and Rockets* **48**, 2011, 187–198.

[20] W. Wüst, Einige Anwendungen des Theorie der Zylinderschale, *Z. Angew. Math. Mech.* **34**, 1954, 444–454.

[21] F.P.J. Rimrott, Querschnittsverformung bei Torsion offener Profile, *Z. Angew. Math. Mech.* **50**, 1970, 775–778.

[22] E.H. Mansfield, Large-deflexion torsion and flexure of initially curved strips, *Proc. R. Soc. Lond.* **A 334**, 1973, 1125–1132.

[23] K.A. Seffen, S. Pellegrino, Deployment dynamics of tape-springs, *Proc. R. Soc. Lond.* **A 455**, 1999, 1003–1048.

[24] K.A. Seffen, On the behaviour of folded tape-springs, *ASME J. Appl. Mech.* **68**, 2001, 369–375.

[25] F. Guinot, S. Bourgeois, B. Cochelin, L. Blanchard, A planar rod model with flexible thin-walled cross-sections. Application to the folding of tape springs, *Int. J. Solids Struct.* **49 (1)**, 2012, 73–86.

[26] E. Picault, P. Marone-Hitz, S. Bourgeois, B. Cochelin, F. Guinot, A planar rod model with flexible cross-section for the folding and the dynamic deployment of tape springs: Improvements and comparisons with experiments, *Int. J. Solids Struct.* **51 (18)**, 2014, 3226–3238.

[27] A. Brinkmeyer, S. Pellegrino, P.M. Weaver, Effects of long-term stowage on the deployment of bistable tape springs, *ASME Journal of Applied Mechanics* **83 (1)**, 2016, 1–11.

[28] K.-W. Kim, Y. Park, Solar array deployment analysis considering path-dependent behavior of a tape spring hinge, *Journal of Mechanical Science and Technology* **29 (5)**, 2015, 1921–1929.

[29] K.-W. Kim, Y. Park, Systematic design of tape spring hinges for solar array by optimization method considering deployment performances, *Aerospace Science and Technology* **46**, 2015, 124–136.

[30] M.K. Kwak, S. Heo, H.B. Kim, Dynamics of satellite with deployable rigid solar arrays, *Multibody System Dynamics* **20 (3)**, 2008, 271–286.

[31] F. Dewalque, J.-P. Collette, O. Brüls, Mechanical behaviour of tape springs used in the deployment of reflectors around a solar panel, *Acta Astronaut.* **123**, 2016, 271–282.

[32] H.M.Y.C. Mallikarachchi, S. Pellegrino, Design of ultrathin composite self-deployable booms, *J. Spacecr. and Rockets* **51**, 2014, 1811–1821.

[33] S. Hoffait, O. Brüls, D. Granville, F. Cugnon, G. Kerschen, Dynamic analysis of the self-locking phenomenon in tape-spring hinges, *Acta Astronaut.* **66**, 2010, 1125–1132.

[34] F. Dewalque, P. Rochus, O. Brüls, Importance of structural damping in the dynamic analysis of compliant deployable structures, *Acta Astronaut.* **111**, 2015, 323–333.

[35] S.J.I. Walker, G. Aglietti, Study of the dynamics of three-dimensional tape spring folds, *AIAA J.* **42**, 2004, 850–856.

[36] S.J.I. Walker, G. Aglietti, Experimental investigation of tape springs folded in three dimensions, *AIAA J.* **44**, 2006, 151–159.

[37] Ö. Soykasap, Analysis of tape spring hinges, *Int. J. Mech. Sci.* **49**, 2007, 853–860.

[38] J.W. Jeong, et al., A novel tape spring hinge mechanism for quasi-static deployment of a satellite deployable using shape memory alloy, *Review of Scientific Instruments* **85**, 2014.

[39] K. Kwok, S. Pellegrino, Viscoelastic effects in tape-springs, in: *52nd AIAA/ASME/ASCE/AHS/ASC Structures, Structural Dynamics and Materials Conference*, Denver, CO, 4-7 April 2011.

[40] Codamotion, Charnwood Dynamics Ltd., Rothley, United Kingdom, `www.codamotion.com`.

[41] Kistler, Kistler Holding AG, Winterthur, Switzerland, `www.kistler.com`.

[42] C. Schwartz, V. Denoël, B. Forthomme, J.-L. Croisier, O. Brüls, Merging multi-camera data to reduce motion analysis instrumental errors using Kalman filters, *Computer Methods in Biomechanics and Biomedical Engineering*, Taylor and Francis **18 (9)**, 952–960, 2015.

[43] The MathWorks, Matlab, 2010, Version 7.10.0 (R2010a).

[44] S.A. Samtech, SAMCEF User Manual, Version 8.4, 2013.

[45] J. Chung, G. Hulbert, A time integration algorithm for structural dynamics with improved numerical dissipation: the generalized-α method, *ASME J. Appl. Mech.* **60**, 1993, 371–375.

[46] R. M. Christensen, Theory of Viscoelasticity: An Introduction, *Academic Press* (New York), 1971.